Anthropogenic intensification of surface ocean interannual pCO2 variability

Angeles Gallego[1], Axel Timmermann[2], Tobias Friedrich[3], and Richard E. Zeebe[3]

[1]Univeristy of Hawaii at Manoa
[2]IBS Center for Climate Physics (ICCP), Pusan National University
[3]University of Hawaii at Manoa

November 22, 2022

Abstract

We use global coupled atmosphere-ocean-biogeochemistry models from the Coupled Model Intercomparison Project (CMIP5), under the RCP8.5 scenario, to show that the global interannual variability of the sea surface pCO (calculated as 1σ) could increase by 62 ± 22 % by 2090. This amplification is a consequence of a larger background pCO and a lower buffering capacity that enhance the response of pCO to surface temperature (T) and dissolved inorganic carbon (DIC) changes.
The amplification is counteracted by a decrease in the sea-surface DIC interannual variability, which will likely cause a strong reduction on the pCO's variability in the equatorial Pacific. The potential changes in seawater carbonate chemistry are simulated with higher consistency than those in the DIC and T anomalies driven by ocean circulation and biology. The changes in sea-surface pCO interannual variability are reflected in the ocean-atmosphere flux of CO and need to be accounted for future carbon projections.

Anthropogenic intensification of surface ocean interannual pCO_2 variability

M. Angeles Gallego[1], Axel Timmermann[2,3], Tobias Friedrich[1], and Richard E. Zeebe[1]

[1]Department of Oceanography, School of Ocean and Earth Sciences and Technology, University of Hawaii at Manoa, Honolulu, Hawaii, USA
[2]Center for Climate Physics, Institute for Basic Science (IBS), Busan, South Korea
[3]Pusan National University, Busan, South Korea

Key Points:

- The sea surface pCO_2 interannual variability is amplified by the end of 21^{st} century in most of the ocean, except in the equatorial Pacific.
- The amplification is due to an increased ocean sensitivity to surface dissolved inorganic carbon and temperature variations.
- A decrease in the dissolved inorganic carbon interannual variability largely counteracts the amplification.

Corresponding author: M. Angeles Gallego, mdla@hawaii.edu

Abstract

We use global coupled atmosphere-ocean-biogeochemistry models from the Coupled Model Intercomparison Project (CMIP5), under the RCP8.5 scenario, to show that the global interannual variability of the sea surface pCO_2 (calculated as 1σ) could increase by 62 ± 22 % by 2090. This amplification is a consequence of a larger background pCO_2 and a lower buffering capacity that enhance the response of pCO_2 to surface temperature (T) and dissolved inorganic carbon (DIC) changes. The amplification is counteracted by a decrease in the sea-surface DIC interannual variability, which will likely cause a strong reduction on the pCO_2's variability in the equatorial Pacific. The potential changes in seawater carbonate chemistry are simulated with higher consistency than those in the DIC and T anomalies driven by ocean circulation and biology. The changes in sea-surface pCO_2 interannual variability are reflected in the ocean-atmosphere flux of CO_2 and need to be accounted for future carbon projections.

Plain Language Summary

We used models to show that the variations in the ocean surface partial pressure of carbon dioxide, that occur between one and ten years, will be larger by the end of the 21^{st} century in most of the ocean. This is because the human carbon emissions make the ocean less able to buffer the natural changes in the total amount of inorganic carbon and temperature that are driven by physics and biology. The models also show that the fluctuations in the total inorganic carbon will be smaller in the future, reducing the variations of the partial pressure of carbon dioxide in the equatorial Pacific. The changes in the ocean's carbon are reflected in the flux of carbon between the atmosphere and the ocean.

1 Introduction

On average, the ocean absorbs 2.4 ± 0.5 Pg of carbon each year (Le Quéré et al., 2018) but this amount varies on interannual time-scales. Efforts have been made to estimate the interannual variability of CO_2 uptake in observations and models (Dong et al., 2017), however there is little agreement with values ranging from ± 0.14 PgC yr^{-1} for 1982-2007 (Park et al., 2010), ± 0.29 1985-2017 (Le Quéré et al., 2018) to ± 0.40 PgC yr^{-1} for 1997-97 (Le Quéré et al., 2000). The CO_2 ocean-atmosphere flux is determined by the difference between ocean and atmospheric pCO_2, and it is further modulated by wind speed variations and sea ice coverage. As the atmospheric pCO_2 is largely uniform around the globe, most of the interannual variability is controlled by the sea surface pCO_2 which is determined by surface dissolved inorganic carbon (DIC), total alkalinity (TA), temperature (T) and salinity (S). Large scale atmosphere-ocean interactions, such as the El Niño Southern Oscillation (ENSO) in the equatorial Pacific, the Pacific Decadal Oscillation (PDO) in the North Pacific, the Southern Annular Mode (SAM) in the Southern Ocean, and the North Atlantic Oscillation (NAO) (McKinley et al., 2004; Friedrich et al., 2006; Landschützer et al., 2019) induce changes in physical circulation and biology that alter DIC, TA, T and S ultimately impacting the CO_2 flux. The effect of DIC, TA, T and S interannual anomalies on the pCO_2 depends on how sensitive the water carbonate chemistry is to these changes. In the ocean, approximately 89% of the dissolved inorganic carbon is in the form of bicarbonate (HCO_3^-) and $\approx$ 10.5% as carbonate (CO_3^{-2}); the CO_2 concentration ($[CO_2]$) only comprises a $\approx$0.5% (Zeebe & Wolf-Gladrow, 2001). As the ocean captures CO_2, its ability to convert it into HCO_3^- and CO_3^{-2} decreases, and the pCO_2 sensitivity to any change in DIC increases. In the same way, a larger background $[CO_2]$ enhances the effect of temperature on pCO_2's solubility. Recently, it was shown that the sea-surface pCO_2 is already experiencing a seasonal amplification (Landschützer et al., 2018; Gorgues et al., 2010) which is projected to increase further according to model projections (Gallego et al., 2018; Fassbender et al., 2017; McNeil & Sasse, 2016; Hauck

& Völker, 2015). Yet the question remains unresolved whether the amplification will also occur for other time-scales. Interannual changes in ocean surface pCO_2 may affect the oceanic sink of anthropogenic CO_2; for example in 2013 the North Pacific subtropical gyre was a net annual source of CO_2 for the first time, due high pCO_2 caused by warm anomalies (Sutton et al., 2017), and during the 2015-2016 El Niño the CO_2 outgassing in the equatorial Pacific was reduced by 26 to 54% (Chatterjee et al., 2017). The current observational time series are not long enough to detect changes in interannual to multi-decadal scales, therefore we rely on Earth System Models (ESMs) to project future changes. Our aim is to quantify how well the CMIP5 models represent the mechanisms of present-day sea surface pCO_2 interannual variability (from now referred as IAV) when compared to data-based estimates, and from there, elucidate the future interannual variability amplification (IAVA) of the carbon cycle in response to greenhouse gases and global warming and the possible consequences for the ocean-atmosphere flux of CO_2.

2 Methodology

Models

For our analysis, sea surface FCO_2, pCO_2, DIC, TA, T and S monthly-mean output variables covering the period from 1861-2005 were obtained from historical simulations, and the period 2006-2100 from future climate change simulations under the Representative Concentration Pathway 8.5 (RCP8.5) (IPCC, 2013). We selected 15 fully coupled earth system models that participated in the Coupled Model Intercomparison Project, Phase 5 (CMIP5) to analyze the standard deviation of pCO_2. Out of the fifteen, we selected six modelsfor a more comprehensive analysis of the causes driving pCO_2 variability; these models were selected based on data availability: CanESM2, CESM1-BGC, GFDL-ESM2M, MPI-ESM-LR, HadGEM2-ES and HadGEM2-CC (See supplementary material of Hauri et al. (2015)). The ocean's surface data sets were regrided onto a 1^ox1^o grid using Climate Data Operators (CDO). The Arctic Ocean and the region poleward of 70^oS are removed from the analyses, because observational data for model validation are scarce.

Analysis

Commonly, the interannual anomalies are defined as deviations of monthly output values from a mean climatology, or by using a running 12 month filter on detrended monthly values. However, for CMIP5 models, the future seasonal cycle of pCO_2 is expected to increase (Gallego et al., 2018), therefore removing a mean climatology for the 1861-2100 period would result in an overestimation of IAVA. On the other hand, a 12 month running filter would remove important sub-annual information and removing a linear trend from a 200-year-long time series poses its own difficulties. To avoid these issues, we calculate the monthly anomalies for each year as the monthly deviation from a 11-year running climatology centered on that year. For example, for the year 1935 we desasonalize the monthly values by subtracting the mean climatology from 1930 to 1940; for the year 1936 we use the climatology from 1931-1941 and so on. (Supplement Figure S1 shows the running climatology for pCO_2 and the anomalies obtained with this method). To elucidate the underlying physical and chemical processes controlling the pCO_2 interannual anomalies (from now pCO_2') we calculated a first order Taylor series expansion of pCO_2' in terms of its four controlling factors, DIC, TA, T and S. To remove the fresh water concentration/dilution effect we use salinity-normalized DIC and TA using a mean salinity of 35 psu, referred as DIC_s and TA_s, (Lovenduski et al., 2007). The freshwater effect is now included in the S_{fw} term. For the Taylor series expansion, each variable (X = DIC_s , TA_s , T and S_{fw}) is decomposed as $X = \overline{X} + X'$. The term $\overline{X}$ represents the running climatology and X' denotes the interannual anomaly. The full first-order series expansion is given by:

$$pCO_2{}' \approx \frac{\partial pCO_2}{\partial DIC}\bigg|_{\overline{TA},\overline{DIC}}{}_{\overline{T},\overline{S}} DIC_s{}' + \frac{\partial pCO_2}{\partial TA}\bigg|_{\overline{TA},\overline{DIC}}{}_{\overline{T},\overline{S}} TA_s{}' + \frac{\partial pCO_2}{\partial T}\bigg|_{\overline{TA},\overline{DIC}}{}_{\overline{T},\overline{S}} T' + \frac{\partial pCO_2}{\partial S}\bigg|_{\overline{TA},\overline{DIC}}{}_{\overline{T},\overline{S}} S'_{fw}, \tag{1}$$

where the derivatives are evaluated on the running climatologies. The full derivation of Eq. (1) is given in the Supplementary material. Equation (1) can be rewritten as:

$$pCO_2{}' \approx \overline{pCO}_2 \cdot \left(\gamma_{DIC_s} \cdot DIC_s{}' + \gamma_{TA_s} \cdot TA_s{}' + \gamma_T \cdot T' + \gamma_S \cdot S_{fw}{}'\right) \tag{2}$$

Where, for notation purposes, each derivative is re-defined as: $\gamma_{\mathrm{X}} = \frac{1}{\overline{\mathrm{pCO}_2}} \cdot \frac{\partial \mathrm{pCO2}}{\partial \mathrm{X}}$, and we will refer to them as the *pCO_2 sensitivity to X*. To determine how much each term contributes to the variability of pCO_2' Equation (2) is mulitplied by $\mathrm{pCO_2}'$, and then averaged, obtaining the following equation:

$$\begin{aligned} < (pCO_2{}')^2 > \;\approx\; & \overline{pCO}_2 \cdot \gamma_{DIC_s} < DIC_s{}' \cdot pCO_2' > \;+\; \overline{pCO}_2 \cdot \gamma_{TA_s} < TA_s{}' \cdot pCO_2' > \\ & \overline{pCO}_2 \cdot \gamma_T \; < T' \cdot pCO_2' > \;+\; \overline{pCO}_2 \cdot \gamma_S < S_{fw}{}' \cdot pCO_2' >, \end{aligned} \tag{3}$$

where $< ... >$ represents a temporal averaging operator. Introducing the following notation:

$$\beta_X \equiv \frac{< \overline{pCO}_2 \cdot \gamma_X \cdot X' pCO_2{}' >}{< (pCO_2')^2 >} \tag{4}$$

, we can then divide Eq. (3) by $< (pCO_2')^2 >$ to give the relationship $\sum_{\mathrm{X}} \beta_{\mathrm{X}} = 1$, where $\mathrm{X} = \{\mathrm{DIC}, \mathrm{TA}, \mathrm{T}, \mathrm{S}\}$, as introduced by Doney et al. (2009). Thus, if we multiply Eq.(4) by the root-mean-square (RMS) of the anomalies (defined as $\sqrt{< (pCO_2{}')^2 >}$), then the β_X coefficients can be interpreted as the fraction of the total pCO_2' RMS that each variable contributes. In our numerical calculations the sum of the β's differs slightly from one due the approximation used for the Taylor expansion, and the anomalies averaged being slightly different from zero.

3 Results

The increase in IAV of surface $\mathrm{pCO_2}'$ is illustrated with the running standard deviation of the monthly anomalies from 1871 to 2090 (Figure 1). The ensemble mean of the globally averaged STD of $\mathrm{pCO_2}$ increases from 6 μatm to 11 μatm by the end of the 21$^{\mathrm{st}}$ century. Detailed global maps of the 1866-1917 and 2045-2095 STD are found in Supplement material S2 and S3. For the $\mathrm{pCO_2}$, a present day comparison shows that the 1987-2010 models STD is about 7 μatm and is larger than the observation-based estimates of $\approx$ 3.2 μatm (Landschützer et al., 2017) (excluding the Arctic region).

Present day sea surface pCO_2 interannual variability

To evaluate the models ability to represent the IAV, we compare the root mean square (RMS) of simulated $\mathrm{pCO_2}'$ for the 1987-2010 period with data-based estimates of Landschützer

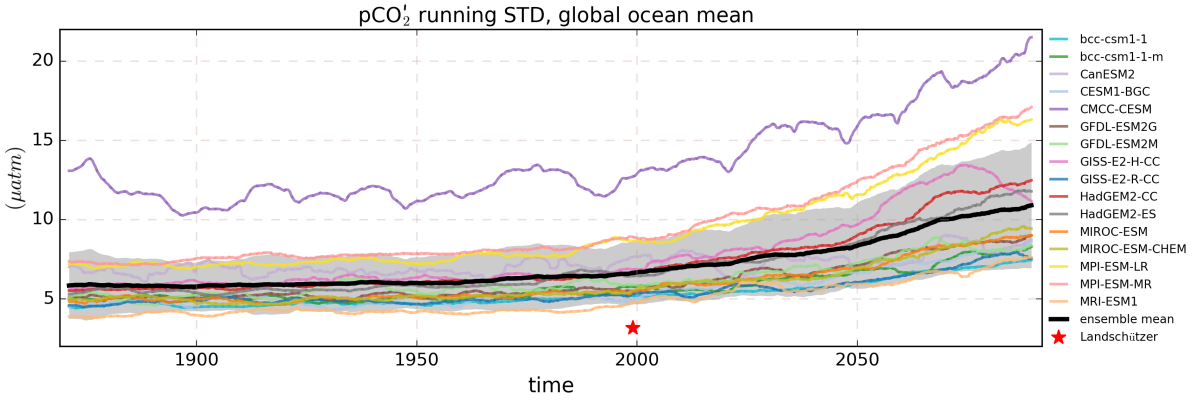

Figure 1. Increase in IAV of the sea surface pCO$_2'$ as a function of time. The IAV is expressed as the running standard deviation (STD) of the monthly anomalies simulated for the historical and the high-emissions Representative Concentration Pathway 8.5 from 1861 to 2100. The STD is calculated using a 10 years moving window for each grid point and then globally averaged. The monthly anomalies for each year were calculated by removing a 11-year climatology centered around that year, in order to remove the positive trend and the increasing seasonal cycle amplitude. The final STD time series comprises the 1871-2090 period. Solid black line indicates the ensemble mean of the individual STDs; the grey area, $\pm 1\sigma$. The STD of the Landschützer et al. (2017) data set for the period 1987-2010 is indicated by a red star.

et al. (2017) (Figure 2, first column). The models CanESM2, CESM1-BGC and GFDL-ESM2M show the largest pCO$_2$ variability in the equatorial Pacific in agreement with the data-based estimates, while for HadGEM2-CC/ES and MPIESM-MR, the strongest fluctuations occur in the high latitudes, especially in the Southern Ocean and North Atlantic. Other observation-based estimates by Rödenbeck et al. (2014) show that the equatorial belt (15°S to 15°N) accounts for 40% of the total temporal standard deviation of the global Ocean. The low equatorial variability in the HadGEM2-CC/ES and MPI-ESM-MR models may be a consequence of the CO$_2$ flux variability that exhibits a much shorter period variation than ENSO time-scales, thus ENSO does not play a dominant role and the high latitudes dominate the variability (Dong et al., 2016).

Models exhibit a higher variability in the subtropical gyres and the high latitudes when compared to the data-based estimate of Landschützer et al. (2017); however the data-based estimations are an interpolation of the Surface Ocean CO$_2$ Atlas (SOCAT) dataset (Bakker et al., 2016; Sabine et al., 2013) which may be biased due to under-sampling, and interpolation methods may cause a lower RMS in high latitudes with limited observational coverage (Landschützer et al., 2019). For example, the data-base product of Rödenbeck et al. (2015), which also uses the SOCAT data, shows lower pCO$_2$ values than mooring time series. This is related to the lack of measurements in some areas and seasons or because moorings are not representative of larger areas (Sutton et al., 2017). In another study, Tjiputra et al. (2014) found that the 1970-2011 deseasonalized pCO$_2$ anomalies of the second release of the SOCAT dataset (Bakker et al., 2014) show a larger standard deviation than the models, but they were of equal magnitude when the models were subsampled to the measurements' areas. The values reported by Landschützer et al. (2019) are lower than the Tjiputra et al. (2014) for all regions. Moreover, the local interannual variability can be much larger when looking at individual time series. For example, Sutton et al. (2014) found that in the Niño 3.4 central equatorial Pacific index region the pCO$_2$ annual mean ranged from 315 to 578 μatm between 1997 and 2011.

The drivers of the $pCO_2{}'$ variability are analyzed in Figure 2 using the decomposition of Eq. (4). Figure 2, columns d, e, f and g show the respective contributions of T, DIC,TA and S to the RMS of the $pCO_2{}'$ for the 1987-2010 period. We compare the results with the Landschützer et al. (2017) estimates for which we calculate only the thermal and non-thermal components (TA and DIC are not available). The non-thermal component comprises the combined contribution of DIC, TA and S, (Takahashi et al., 2002). The thermal and non-thermal contributions calculated for the CMIP5 models can be found in Supplement material (Figure S4); these follow the DIC and T patterns. The regional dominance of the thermal and non-thermal components on the IAV emulates that of its seasonal cycle; the high latitudes, and the strong upwelling region of equatorial Pacific are dominated by non-thermal changes; whereas the subtropical gyres are controlled by the solubility changes induced by temperature variations (Landschützer et al., 2019). In the equatorial Pacific, HadGEM2-CC/ES and MPIESM-MR show that during El Niño years the pCO_2 anomalies are positive due to increased temperatures induced by the anomalous eastward advection of warmer waters; while CanESM2, CESM1-BGC and GFDL-ESM2M suggest that the redistribution of oceanic currents and reduced upwelling of DIC-rich waters generates negative pCO_2 anomalies (Jin et al., 2019). The DIC-dominated models are in agreement with results obtained from observations (Feely et al., 2006; Sutton et al., 2014), an offline model driven by reanalysis ocean products (Valsala et al., 2014) and a hindcast simulation (Doney et al., 2009). The observed $pCO_2{}'$ associated with El Niño are negative and are predominantly caused by wind driven changes in the currents that alter the DIC distribution, rather than by changes in temperature (Doney et al., 2009; Valsala et al., 2014; Long et al., 2013; Feely et al., 1999; Cosca et al., 2003). The models that fail to represent the dominance of DIC on pCO_2 IAV in the equatorial Pacific, present a weak reduction in upwelling during El Niño years and weak vertical gradients of DIC (Jin et al., 2019). In the equatorial Atlantic region only the HadGEM2-CC/ES shows a temperature dominance (Wang et al., 2015), disagreeing with the Landschützer et al. (2019) estimate. Only the HadGEM2-CC/ES model shows a relatively important alkalinity contribution in the North Atlantic and North Pacific that counteracts the positive DIC contribution. Salinity has a minor effect everywhere, with a small positive effect in the western Pacific associated with rainfall changes due ENSO. Models agree with the data estimates on the non-thermal dominance in the high latitudes (Figure 2). The Southern Ocean pCO_2's IAV is the result of increased upwelling of DIC-rich waters caused by stronger winds related to the southern annular mode (Resplandy et al., 2015; Verdy et al., 2007). In the sub-polar North Atlantic the observations show a non-thermal dominance north of 40°N, while in the models the DIC dominance extends to 25-30 °N.

Future sea surface pCO_2 interannual variability

The sea surface pCO_2 IAV, calculated as the RMS-value of the interannual pCO_2 anomalies, is amplified in most of the ocean by the end of the 21^{st} century (Figure 3a), (see Supplement material Figure S5 for each individual model). Yet, the magnitude of the IAV amplification (IAVA) exhibits large regional differences, and even decreases in the equatorial Pacific for some models. Here, we analyze the causes of IAVA and its spatial heterogeneity by separating the analysis into two groups of models according to their behavior. The first group includes the CanESM2, CESM1-BGC and GFDL-ESM2G. They exhibit the maximum IAV in the equatorial Pacific, which decreases in the future and is dominated by DIC (see Figure 3a, upper row). The second group includes the HadGEM2-CC/ES and MPI-ESM-lR models, and is characterized by maximum IAV in the high latitudes (especially in the Southern Ocean), a temperature dominance in the equatorial Pacific's IAV and an increase in future IAV everywhere (see Figure 3a, bottom row). The same behavior is observed in the ocean-atmosphere CO_2 flux (FCO_2) (Figure 3c). The pattern correlation between the change on RMS of pCO_2' and the change on RMS of FCO_2' is in the order of 0.5 to 0.8 depending on the model (not shown). This indicates that increased pCO_2 IAV is one of the main drivers of the FCO_2 IAV increase. However, ad-

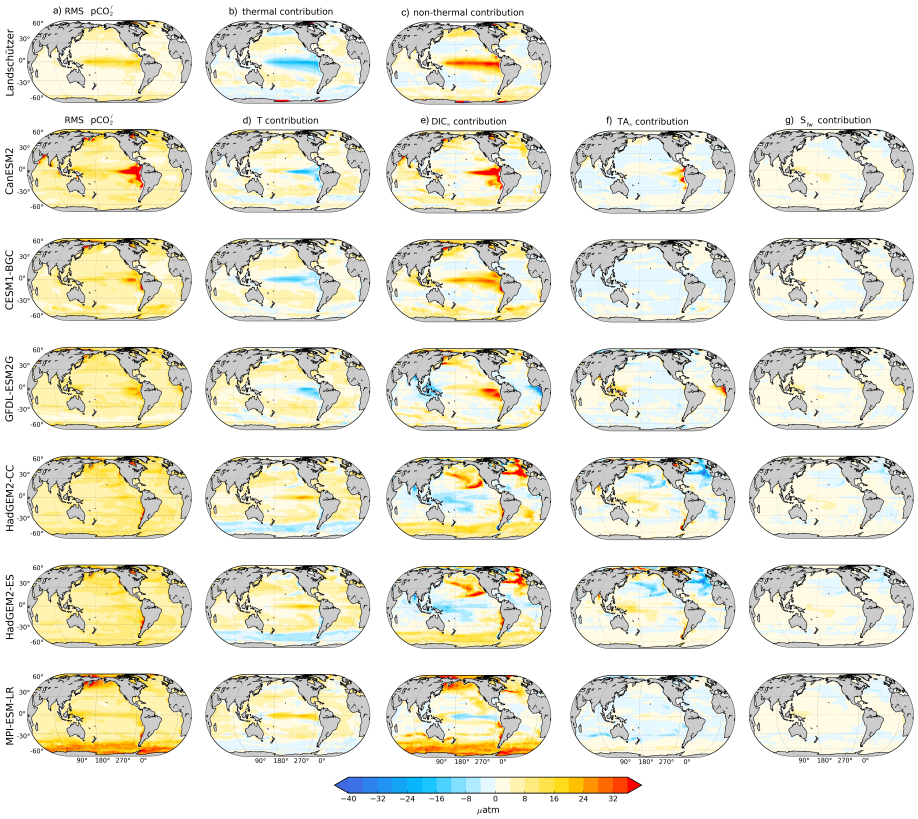

Figure 2. Mechanisms driving the 1987-2010 interannual variability of surface ocean pCO_2. First row shows the **a)** Landschützer et al. (2017) estimate of the root mean square (RMS) of pCO_2 interannual anomalies, and its **b)** thermal and **c)** non-thermal contributions. Panels on the second to seventh rows show the different CMIP5 models **a)** root mean square (RMS) of pCO_2 interannual anomalies and its contributions from **d)** temperature (T), **e)** salinity normalized dissolved inorganic carbon (DIC_s), **f)** salinity normalized total alkalinity (TA_s) and **g)** salinity incldluing fresh water effect (S_{fw}). For the observations, we calculate a thermal and non-thermal terms following Takahashi et al. (2002) method because there is not enough DIC, TA and S data available. The non-thermal component comprises the combined effects of DIC, TA and S. Following the method of Doney et al. (2009), each map of the contributions is calculated as the β coefficient of Eq. (4) normalized by the RMS of the pCO_2'. In the panels, yellow-redish colors indicate a positive contribution to the RMS of pCO_2 interannual anomalies and blue colors represent a negative contribution.

ditional substantial contributions coming from changes in wind speed and solubility also play a role.

We now set to determine how much of the pCO_2 IAVA is due to changes in mean background carbonate chemistry and how much can be explained by changes in physical and biological processes. To this aim, we calculate the RMS of ${pCO_2}'$ for the final period as if only the background carbonate chemistry - represented by $p\overline{CO}_2$ and the sensitivities (γ_T and γ_{DIC})- increase, but maintaining the initial values of the anomalies given by T′ and ${DIC_s}'$ (see Eq. (2)). The later anomalies are the result of physical and biological variations. In both groups of models, the case in which only the carbonate chemistry is changed shows a global mean IAVA 3.4 times larger than for the case in which ${DIC_s}'$ and T′ are also allowed to vary (compare in Figure 3b with 3a). The large increase in $p\overline{CO}_2$ and γ_{DIC} is similar for both groups of models and generate an overall amplification (Figure 4a,b). It is important to mention that the separation between $p\overline{CO}_2$ and γ_{DIC_s} is a mathematically construct rather than two separate phenomena. Ultimately, the change in $p\overline{CO}_2 \cdot \gamma_{DIC_s}$ is what determines the increase in the DIC contribution, while the T contribution increases almost exclusively due to the increase in $p\overline{CO}_2$ since γ_T remains almost unchanged (not shown).

The damping of the pCO_2 IAVA in the case where both, carbon chemistry and interannual anomalies change is due to a decrease of the DIC′ interannual variability (Figure 4a). The simulations differ in DIC′ creating a large spread in the projected IAVA. For example, in the first group of models, the DIC standard deviation has a maximum in the equatorial Pacific and decreases in the future by ≈41% causing a decrease in pCO_2 IAV in the region (Figure 4c). For the MPI-ESM-LR and HadGEM-ES/CC the DIC anomalies are smaller in the equatorial region but increase by ≈8% , enhancing the IAVA. In high latitudes, the DIC STD decreases for both groups of models, but they present a larger sensitivity and a more rapid increase in $\overline{pCO}_2$ than the mid-low latitudes (Figure 4a,b), which agrees with previous studies (Bates et al., 2014; Egleston et al., 2010). Of the two groups of models, the MPI-ESM-LR and HadGEM-ES/CC show a smaller decrease in DIC′ and a larger increase in the sensitivity, and therefore result in a larger pCO_2 IAVA than the CanESM2, CESM1-BGC and GFDL-ESM2G. Interestingly, the T′ anomalies remain of similar magnitude during both periods of time, which makes the overall T contribution to pCO_2 be more amplified than the DIC contribution (see Supplement material, Figure S6).

The intra-model differences on DIC′ and T′ IAV arise from the differences in physical and biological controls, or due to changes in the main modes of ocean-atmosphere variability, such as ENSO, NAO, SAM and PDO. An in-depth analysis of these causes is beyond the scope of this paper, but we discuss some possible explanations found in the current literature. One of the reasons for the diminished DIC′ variability under future emission scenarios, may be related to the fact that climate models simulate a weaker Walker circulation in response to global warming (Vecchi et al., 2006; Zhao & Allen, 2019); this would weaken the upwelling of DIC-rich waters during La Niña conditions.Other studies suggest a future increase in ENSO amplitude and a weakening of the Walker circulation, will increase the frequency of the eastward propagation of warm waters (Timmermann et al., 1999; Cai et al., 2015, 2018). Moreover, Cai et al. (2018) found that models that accurately represent the ENSO features, also show a future increase in ENSO's frequency; this indicates that the reduction of DIC variability cannot be controlled solely by changes in the climate modes of variability. However, the recent strengthening of the trade winds and the unresolved models biases make these projections of medium confidence (Cai et al., 2015; Timmermann et al., 2018).

Another possible explanation for the diminished DIC′ variability is the projected shoaling of the winter mixed layer depth, associated with a reduced heat loss during the cold season. The mixed layer shoaling will cause less mixing of deep rich DIC waters to the surface on both, seasonal and interannual timescales. In the winter deep convection

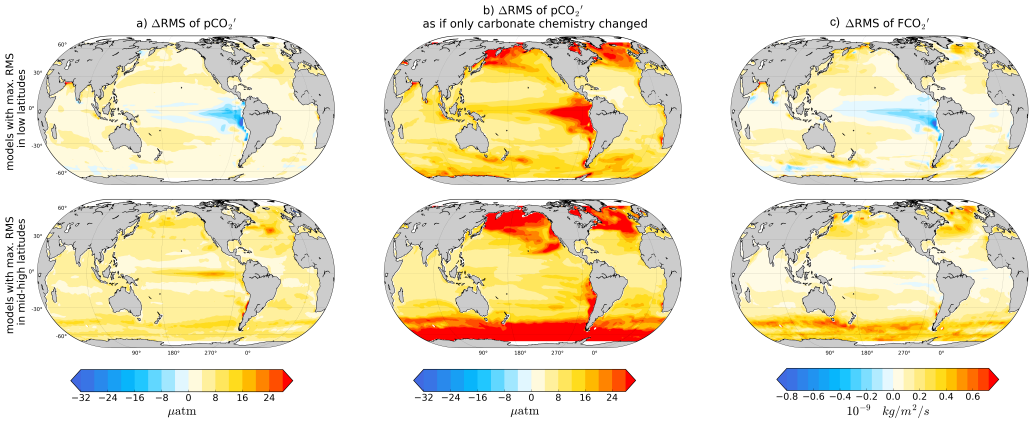

Figure 3. Causes of increasing sea surface pCO_2' variability: Total change (measured as 2045-2095 minus 1870-1920 values) of **a)** the RMS of pCO_2', **b)** RMS of pCO_2' when only the value of $\overline{pCO_2}$, γ_{DIC_s} and γ_T vary, but we keep constant the 1870-1920 value of the DIC_s' and T' interannual anomalies and **c)** the RMS of FCO_2'. First we compute the total change for each model and subsequently take the ensemble mean of CanESM2, CESM1-BGC and GFDL-ESM2G **(top row)** and HadGEM-CC/ES and MPI-ESM-LR **(bottom row)**. Panel **b)** highlights that the RMS of pCO_2 increases due carbonate chemistry changes. However, the interannual variability of DIC and T generates differences between column a) and b) that depend on the models' physical and biological dynamics.

regions the future shoaling of the MLD may be underestimated by models, because they show a shallower than observed present-day mixed layer depth (Downes et al., 2009; Sallée et al., 2013). Simulations show that a decrease in mixed layer depth will also reduce the input of macronutrients and therefore reduce primary productivity, this may be reflected in a reduced DIC variability (Bopp et al., 2013). In other areas, such as the Southern Ocean, a reduction in the light and temperature limitation prove to increase primary productivity (Steinacher et al., 2010) which could counteract the decrease of the DIC variability in these regions associated with shallower MLD. The total reduction of the DIC STD may be a combination of these factors; for example, even if ENSO magnitude and frequency were to increase, a reduction of the MLD may confine the ocean uptake of CO_2 to the surface, thereby reducing the DIC vertical gradient. As a result frequent upwelling events would have a smaller impact on pCO_2.

4 Summary and Conclusions

The ocean surface pCO_2 responds to climate modes of variability that alter the ocean's circulation and biogeochemical conditions on interannual time-scales (Resplandy et al., 2015). Two opposing mechanisms control future changes in pCO_2 IAVA; a higher background CO_2 concentration together with an increased sensitivity to DIC that enhances the pCO_2 response to changes in T and DIC, and a reduction of the DIC' IAV that counteracts the pCO_2 IAVA. In the end, although DIC' changes will be smaller compared to present-day, the ocean will be much more sensitive to them, resulting in an overall pCO_2' variability increase in most of the global ocean.

The future pCO_2 interannual response to greenhouse gases varies with latitude; most models show that the high latitudes with large pCO_2 IAV are also the ones that will be exposed to larger amplification, because the buffering capacity decreases faster in this region (Egleston et al., 2010). The mid-latitudes variability will be mildly amplified by

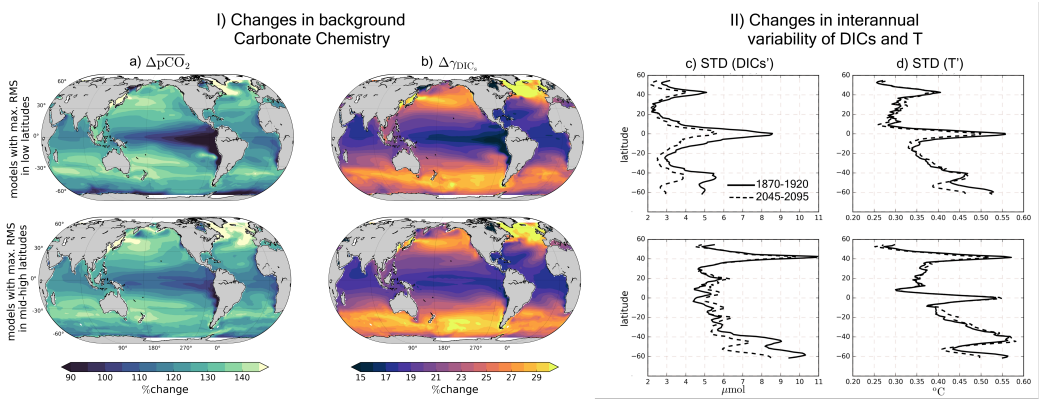

Figure 4. Changes in carbonate chemistry and interannual variability of surface DIC_s' and T′. Percentage change (measured as 2045-2095 minus 1870-1920 values) of **a)** $\overline{pCO_2}$ and **b)** γ_{DIC_s}. A 100% change indicates a doubling in magnitude. **c)** and **d)** show the ensemble mean of the zonally averaged standard deviation of DIC_s' and T′ respectively. The **top** row shows the ensemble mean for models CanESM2, CESM1-BGC and GFDL-ESM2G and the **bottom** for HadGEM-CC/ES and MPI-ESM-LR.

a larger pool of CO_2 that magnifies the response to T variability. In the equatorial Pacific the models show a larger discrepancy; the models that agree with present-day observations project a decrease in equatorial pCO_2 IAV due to the reduction of the DIC′ variability that overcompensates the increased DIC sensitivity. On the other hand, the HadGEM2-CC/ES and MPI-ESM-LR models show a future small increase in this region, because their pCO_2 IAV is dominated by T instead of DIC.

An unresolved issue is how a future increase in CO_2 emissions will affect the CO_2 flux budget. We showed that the FCO_2 anomalies also experience an increase in variability, that follows the pattern of the pCO_2 IAVA but is modulated by wind speed and solubility variations not accounted for in the present work. The FCO_2 IAVA disagree with the result of Dong et al. (2016) who found no increase in FCO_2 IAV on the CMIP5 models. The reason behind this discrepancy is that Dong et al. (2016) compared the STD of the FCO_2 anomalies between pre-industrial and present day levels, while we compared the end of the century levels with those at the onset of the industrial revolution. The increase in IAV is gradual and remains small at the beginning of the 21st. Therefore, longer time series are needed to detect the amplification. In another study, Keller et al. (2015) studied ENSO variability in CESM1-BGC for the 850-2100 period, the authors found that the warmest period had the lowest variance in ENSO, and that the air-sea CO_2 flux response was the lowest. The later result agrees with our finding that the pCO_2 variability decreases in the eastern equatorial Pacific for this model.

Changes of surface ocean pCO_2 on interannual time scales not only affect the source/sink nature of the ocean, but also they may generate in the high latitudes acidification and hypercapnia episodes on interannual time-scales (McNeil & Sasse, 2016; Sasse et al., 2015). In the mean time, future projections rely on ocean models as the current datasets are sparse and lack time continuity. The model's differences and similarities highlight the large gap in knowledge about the complex physical and biological factors modulated by ocean-atmosphere interactions that control the interannual variability, but also prove the undeniable consequences of the changing background carbonate chemistry.

Acknowledgments

This work was supported by the National Science Foundation under Grant No. 1314209. A.T is supported by the Institute for Basic Science (IBS), South Korea under IBS-R028-D1. R.E.Z. acknowledges support from the US NSF (OCE15-58699). The CMIP5 data used in the analysis were obtained from https://esgf-node.llnl.gov/projects/esgf-llnl/ (last access: June 2019; Taylor et al. (2012)). The Landschützer et al. (2017) pCO_2 data product is available at https://www.nodc.noaa.gov/archive/arc0105/0160558/3.3/data/0-data/ (last access: June 2019).

References

Bakker, D. C. E., Pfeil, B., Landa, C. S., Metzl, N., O'Brien, K. M., Olsen, A., ... et al. (2016). A multi-decade record of high-quality fCO_2 data in version 3 of the Surface Ocean CO_2 Atlas (SOCAT). *Earth Syst. Sci. Data*, *8*, 383-413.

Bakker, D. C. E., Pfeil, P., Smith, K., Hankin, S., Olsen, A., & et al. (2014). An update to the Surface Ocean CO_2 Atlas (SOCAT version 2). *Earth Syst. Sci. Data*, *6*, 69-90.

Bates, N. R., Astor, Y. M., Church, M. J., Currie, K., Dore, J. E., Gonzalez-Davila, M., ... Santana-Casiano, J. M. (2014). A Time-Series View of Changing Ocean Chemistry Due to Ocean Uptake of Anthropogenic CO_2 and Ocean Acidification. *Oceanopgraphy*, *27(1)*, 126-141.

Bopp, L., Resplandy, L., Orr, J. C., Doney, S. C., Dunne, J. P., Gehlen, M., ... Vichi, M. (2013). Multiple stressors of ocean ecosystems in the 21st century: projections with CMIP5 models. *Biogeosciences*, *10*, 6225–6245.

Cai, W., Santoso, A., Wang, G., Yeh, S., An, S., Cobb, K. M., & et al. (2015). ENSO and greenhouse warming. *Nature Climate Change*, *5*, 849-859.

Cai, W., Wang, G., Dewitte, B., Wu, L., Santoso, A., Takahashi, K., ... McPhaden, M. J. (2018). Increased variability of eastern Pacific El Niño under greenhouse warming. *Nature*, *564*(7735), 201–206. Retrieved from `https://doi.org/10.1038/s41586-018-0776-9` doi: 10.1038/s41586-018-0776-9

Chatterjee, A., Gierach, M. M., Sutton, A. J., Feely, R. A., Crisp, D., Eldering, A., ... Schimel, D. S. (2017). Influence of El Niño on atmospheric CO_2 over the tropical Pacific Ocean: Findings from NASA's OCO-2 mission. *Science*, *358*(6360).

Cosca, C. E., Feely, R. A., Boutin, J., Etcheto, J., & McPhaden, M. J. (2003). Seasonal and interannual CO_2 fluxes for the central and eastern equatorial Pacific Ocean as determined from fCO_2-SST relationships. *J. Geophys. Res.*, *108(C8)*(3278).

Dickson, A. G. (1990). Thermodynamics of the dissociation of boric acid in synthetic seawater from 273.15 to 318.15 K. *Deep-Sea Research Part A. Oceanographic Research Papers*, *37*, 755–766.

Doney, S. C., Lima, I., Feely, R. A., Glover, D. M., Lindsay, K., Mahowald, N., ... Wanninkhof, R. (2009). Mechanisms governing interannual variability in upper-ocean inorganic carbon system and air–sea CO_2 fluxes: Physical climate and atmospheric dust. *Deep Sea Research Part II: Topical Studies in Oceanography*, *56*(8), 640 - 655. doi: https://doi.org/10.1016/j.dsr2.2008.12.006

Dong, F., Li, Y., & Wang, B. (2017). Assessment of responses of tropical Pacific air-sea CO_2 flux to ENSO in 14 CMIP5 models. *Journal of Climate*, *30*, 8595-8613.

Dong, F., Li, Y., Wang, B., Huang, W., Shi, Y., & Dong, W. (2016). Global Air-Sea CO_2 Flux in 22 CMIP5 Models: Multiyear Mean and Interannual Variability. *Journal of Climate*, *29*(7), 2407-2431.

Downes, S. M., Bindoff, N. L., & Rintoul, S. R. (2009). Impact of climate change on the subduction of mode and intermediate water masses in the Southern Ocean.

Journal of Climate, *22*, 3289-3302.

Egleston, E. S., Sabine, C. L., & Morel, F. M. M. (2010). Revelle revisited: Buffer factors that quantify the response of ocean chemistry to changes in DIC and alkalinity. *Global Biogeochem. Cycles*, *24*, GB1002.

Fassbender, A. J., Sabine, C. L., & Palevsky, H. I. (2017). Nonuniform ocean acidification and attenuation of the ocean carbon sink. *Geophysical Reserach Letters*, *44*, 8404–8413.

Feely, R. A., Takahashi, T., Wanninkhof, R., McPhaden, M. J., Cosca, C. E., Sutherland, S. C., & Carr, M. E. (2006). Decadal variability of the air-sea CO_2 fluxes in the equatorial Pacific Ocean. *J. Geophys. Res.*, *111*(C08S90).

Feely, R. A., Wanninkhof, R., Takahashi, T., & Tans, P. (1999). Influence of El-Niño on the Equatorial Pacific contribution to atmospheric CO_2 accumulation. *Nature*, *398*, 597-601.

Friedrich, T., Oschlies, A., & Eden, C. (2006). Role of wind stress and heat fluxes in generating interannual-to-decadal variability of air-sea CO_2 and O_2 fluxes in a North Atlantic model. *Geophysical Reserach Letters*, *33*(LS21S04).

Gallego, M. A., Timmermann, A., Friedrich, T., & Zeebe, R. E. (2018). Drivers of future seasonal cycle changes in oceanic pCO_2. *Biogeosciences*, *15*, 5315-5327.

Gorgues, T., Aumont, O., & Rodgers, K. B. (2010). A mechanistic account of increasing seasonal variations in the rate of ocean uptake of anthropogenic carbon. *Biogeosciences*, *7*, 2581–2589.

Hauck, J., & Völker, C. (2015). Rising atmospheric CO_2 leads to large impact of biology on Southern Ocean CO_2 uptake via changes of the Revelle factor. *Geophysical Reserach Letters*, *42*, 1459–1464.

Hauri, C., Friedrich, T., & Timmermann, A. (2015). Abrupt onset and prolongation of aragonite undersaturation events in the Southern Ocean. *Nat. Clim. Change*, *6*, 172–176.

IPCC. (2013). *IPCC Climate Change 2013: The Physical Science Basis. Contribution of Working Group i to the Fifth Assessment Report of the Intergovernmental Panel on Climate Change.* Cambridge, United Kingdom and New York, NY, USA: Cambridge University Press.

Jin, C., Zhou, T., & Chen, X. (2019). Can CIMP5 Earth System Models reproduce the interannual variability of air-sea CO_2 fluxes over the tropical Pacific Ocean? *J. Climate*, *32*, 2261-2275.

Keller, K. M., Joos, F., Lehner, F., & Raible, C. C. (2015). Detecting changes in marine responses to ENSO from 850 to 2100 C.E.: Insights from the ocean carbon cycle. *Geophysical Reserach Letters*, *42*.

Landschützer, P., Gruber, N., & Bakker, D. (2017). *An updated observation-based global monthly gridded sea surface pCO_2 and air-sea CO_2 flux product from 1982 through 2015 and its monthly climatology (NCEI Accession 0160558). Version 2.2. NOAA National Centers for Environmental Information. Dataset. doi:10.7289/v5z899n6.*

Landschützer, P., Gruber, N., Bakker, D. C. E., Stemmler, I., & Six, K. D. (2018). Strengthening seasonal marine CO_2 variations due to increasing atmospheric CO_2. *Nat. Clim. Change*, *8*, 146–150.

Landschützer, P., Ilyina, T., & Lovenduski, N. (2019). Detecting regional modes of variability in observation-based surface ocean pCO_2. *Geophysical Reserach Letters*, *46*, 2670-2679.

Le Quéré, C., Andrew, R. M., Friedlingstein, P., Sitch, S., Hauck, J., Pongratz, J., et al. (2018). Global carbon budget 2018. *Earth Syst. Sci. Data Discuss*(1-3).

Le Quéré, C., Orr, J. C., Monfray, P., & Aumont, O. (2000). Interannual variability of the oceanic sink of CO_2 from 1979 through 1997. *Global Biogeochem. Cycles*, *14*(4), 1247-1265.

Long, M., Lindsay, K., Peacock, S., Moore, J. K., & Doney, S. C. (2013). Twentieth-century oceanic carbon uptake and storage in CESM1(BGC). *J. Climate*, *26*,

6775-6800.

Lovenduski, N. S., Gruber, N., Doney, S. C., & Lima, I. D. (2007). Enhanced CO_2 outgassing in the Southern Ocean from a positive phase of the Southern Annular Mode. *Global Biogeochem. Cycles*, *21*, GB2026.

McKinley, G. A., Follows, M. J., & Marshall, J. (2004). Mechanisms of air-sea CO_2 flux variability in the equatorial Pacific and the North Atlantic. *Global Biogeochem. Cycles*, *18*(GB2011).

McNeil, B. I., & Sasse, T. P. (2016). Future ocean hypercapnia driven by anthropogenic amplification of the natural CO_2 cycle. *Nature*, *529*, 383–386.

Millero, F. J. (1995). Thermodynamics of the carbon dioxide system in the oceans. *Geochemica et Cosmochemica Acta*, *59*, 661–677.

Millero, F. J., Graham, T. B., Huang, F., Bustos-Serrano, H., & Pierrot, D. (2006). Dissociation constants of carbonic acid in seawater as a function of salinity and temperature. *Marine Chemistry*, *100(1–2)*, 80–94.

Park, G. H., Wanninkhof, R., Doney, S. C., Takahashi, T., Lee, K., Feely, R. A., ... Triñanes, J. (2010). Variability of global net sea–air CO_2 fluxes over the last three decades using empirical relationships. *Tellus B*, *62B*, 352-368.

Resplandy, L. R., Séférian, R., & Bopp, L. (2015). Natural variability of CO_2: What can we learn from centuries-long climate models simulations? *J. Geophys. Res. Oceans*, *120*, 384-404.

Rödenbeck, C., Bakker, D., Metzl, N., Olsen, A., Sabine, C., Cassar, N., ... Heimann, M. (2014). Interannual sea–air CO_2 flux variability from an observation-driven ocean mixed-layer scheme. *Biogeosciences*, *11*, 4599-4613.

Rödenbeck, C., Bakker, D. C. E., Gruber, N., Iida, Y., Jacobson, A. R., Jones, S., ... Zeng, J. (2015). Data-based estimates of the ocean carbon sink variability – first results of the Surface Ocean pCO_2 Mapping intercomparison (SOCOM). *Biogeosciences*, *12*, 7251-7278.

Sabine, C. L., Hankin, S., Koyuk, H., Bakker, D. C. E., Pfeil, B., Olsen, A., ... others (2013). Surface Ocean CO_2 Atlas (SOCAT) gridded data products. *Earth Syst. Sci. Data*, *5*, 145-153.

Sallée, J. B., Shuckburgh, E., Bruneau, N., Meijers, A. J. S., Bracegirdle, T. J., & Wang, Z. (2013). Assessment of Southern Ocean mixed-layer depths in CMIP5 models: Historical bias and forcing response. *Geophysical Research Oceans*, *118*, 1845-1862.

Sasse, T., McNeil, B. I., Matear, R., & Lenton, A. (2015). Quantifying the influence of CO_2 seasonality on future aragonite undersaturation onset. *Biogeosciences*, *12*, 6017-6031.

Steinacher, M., Joos, F., Froelicher, T. L., Bopp, L., Cadule, P., Cocco, V., ... Segschneider, J. (2010). Projected 21st century decrease in marine productivity: a multi-model analysis. *Biogeosciences*, *7*, 979–1005.

Sutton, A. J., Feely, R. A., Sabine, C. L., McPhaden, M. J., Takahashi, T., Chavez, F. P., ... Mathis, J. T. (2014). Natural variability and anthropogenic change in equatorial Pacific surface ocean pCO_2 and pH. *Global Biogeochem. Cycles*, *28*, 131-145.

Sutton, A. J., Wanninkhof, R., Sabine, C. L., Feely, R. A., Cronin, M. F., & Weller, R. A. (2017). Variability and trends in surface seawater pCO_2 and CO_2 flux in the Pacific Ocean. *Geophysical Reserach Letters*, *44*, 5627-5636.

Takahashi, T., Sutherland, S. C., Sweeney, C., Poisson, A., Metzl, N., Tilbrook, B., ... Nojiri, Y. (2002). Global sea-air CO_2 flux based on climatological surface ocean pCO_2, and seasonal biological and temperature effects. *Deep-Sea Research II*, *49*, 1601–1623.

Taylor, K. E., Stouffer, R. J., & Meehl, G. A. (2012). An Overview of CMIP5 and the experiment design, B. *Am. Meteorol. Soc.*, *93*, 485-489.

Timmermann, A., An, S., Kug, J., Jin, F., Cai, W., Capotondi, A., ... et al. (2018). El Niño–Southern Oscillation complexity. *Nature*, *559*(7715), 535-543.

Timmermann, A., Oberhuber, J., Bacher, A., Esch, M., Latif, M., & Roeckner, E. (1999). Increased El Niño frequency in a climate model forced by future greenhouse warming. *Nature*, *398*(6729), 694-697.

Tjiputra, J. F., Olsen, A. R. E., Bopp, L., Lenton, A., Pfeil, B., Roy, T., ... Heinze, C. (2014). Long-term surface pCO_2 trends from observations and models. *Tellus B*, *66*(23083).

Valsala, V. K., Roxy, M. K., Ashok, K., & Murtugudde, R. (2014). Spatiotemporal characteristics of seasonal to multidecadal variability of pCO_2 and air-sea CO_2 fluxes in the equatorial Pacific Ocean. *J. Geophys. Res. Oceans*, *119*, 8987–9012.

Vecchi, G. A., Soden, B. J., Wittenberg, A. T., Held, I. M., & Leetmaa, A. (2006). Weakening of tropical Pacific atmospheric circulation due to anthropogenic forcing. *Nature*, *441*, 73-76.

Verdy, A., Dutkiewicz, S., Follows, M. J., Marshall, J., & Czaja, A. (2007). Carbon dioxide and oxygen fluxes in the Southern Ocean: Mechanisms of interannual variability. *Global Biogeochem. Cycles*, *21*(GB2020).

Wang, X., Murtugudde, R., Hackert, E., Wang, J., & Beauchamp, J. (2015). Seasonal to decadal variations of sea surface pCO_2 and sea-air CO_2 flux in the equatorial oceans over 1984–2013: A basin-scale comparison of the Pacific and Atlantic Oceans. *Global Biogeochem. Cycles*.

Zeebe, R. E., & Wolf-Gladrow, D. (2001). *CO_2 in Seawater: Equilibrium, Kinetics, Isotopes*. Amsterdam, Netherlands, and Philadelphia, PA, USA: Elsevier Science.

Zhao, X., & Allen, R. J. (2019). Strengthening of the Walker Circulation in recent decades and the role of natural sea surface temperature variability. *Environ. Res. Commun*, *1*(021003).

Supporting Information for "Anthropogenic intensification of surface ocean interannual pCO_2 variability"

M. Angeles Gallego[1], Axel Timmermann[2,3], Tobias Friedrich[1], and Richard E. Zeebe[1]

[1]Department of Oceanography, School of Ocean and Earth Sciences and Technology, University of Hawaii at Manoa, Honolulu, Hawaii, USA

[2]Center for Climate Physics, Institute for Basic Science (IBS), Busan, South Korea

[3]Pusan National University, Busan, South Korea

Contents of this file

1. Text S1

2. Figures S1 to S6

Introduction

Text S1.

We construct the full pCO_2 Taylor's expansion decomposition starting with the carbonate chemistry definitions of DIC and TA as in Egleston, Sabine, and Morel (2010):

$$DIC = [CO_2] + \frac{K_1[CO_2]}{[H^+]} + \frac{K_1K_2[CO_2]}{[H^+]^2} \tag{1}$$

$$TA = \frac{K_1[CO_2]}{[H^+]} + 2\frac{K_1K_2[CO_2]}{[H^+]^2} + \frac{B_{tot}K_b}{(K_b + [H^+])} - [H^+] + \frac{K_w}{[H^+]} \tag{2}$$

Where K_1 and K_2 are defined as Millero, Graham, Huang, Bustos-Serrano, and Pierrot (2006), K_w as Millero (1995) and K_b according to Dickson (1990). From Eq. (1) we can obtain $[H^+]$ and from Eq. (2) we get $[CO_2]$ respectively as:

$$[H^+] = \frac{K_1[CO_2] + \sqrt{K_1^2[CO_2]^2 + 4K_1K_2[CO_2](DIC - [CO_2])}}{2(DIC - [CO_2])} \tag{3}$$

$$[CO_2] = \frac{[H^+]^2}{K_1[H^+] + 2K_1K_2}\Big(TA - \frac{B_{tot}K_b}{(K_b + [H^+])} + [H^+] - \frac{K_w}{[H^+]}\Big) \tag{4}$$

For $[H^+]$ the positive solution was chosen; the negative root gives a result far from real values. From Eq. (3) and Eq. (4) we can make a Taylor's expansion of $[H^+]$ and $[CO_2]$ respectively as:

$$\delta[H^+] = \frac{\partial[H^+]}{\partial DIC}\Big|_{\substack{\overline{CO_2},\overline{DIC} \\ \overline{T},\overline{S}}}\delta DIC + \frac{\partial[H^+]}{\partial[CO_2]}\Big|_{\substack{\overline{CO_2},\overline{DIC} \\ \overline{T},\overline{S}}}\delta[CO_2] + \frac{\partial[H^+]}{\partial T}\Big|_{\substack{\overline{CO_2},\overline{DIC} \\ \overline{T},\overline{S}}}\delta T + \frac{\partial[H^+]}{\partial S}\Big|_{\substack{\overline{CO_2},\overline{DIC} \\ \overline{T},\overline{S}}}\delta S \tag{5}$$

$$\delta[CO_2] = \frac{\partial[CO_2]}{\partial TA}\Big|_{\substack{\overline{TA},\overline{H} \\ \overline{T},\overline{S}}}\delta TA + \frac{\partial[CO_2]}{\partial[H^+]}\Big|_{\substack{\overline{TA},\overline{H} \\ \overline{T},\overline{S}}}\delta[H^+] + \frac{\partial[CO_2]}{\partial T}\Big|_{\substack{\overline{TA},\overline{H} \\ \overline{T},\overline{S}}}\delta T + \frac{\partial[CO_2]}{\partial S}\Big|_{\substack{\overline{TA},\overline{H} \\ \overline{T},\overline{S}}}\delta S \tag{6}$$

The overbars indicate the climatologies of the variables in which the derivatives are evaluated. Finally, we insert $\delta[H^+]$ from Eq. (5) into Eq. (6), to get $[CO_2]$ in terms of DIC, TA, T and S:

$$\begin{aligned}\delta[CO_2] = {} & \left[1 - \frac{\partial[CO_2]}{\partial[H^+]}\Big|_{\substack{\overline{TA},\overline{H} \\ \overline{T},\overline{S}}}\frac{\partial[H^+]}{\partial[CO_2]}\Big|_{\substack{\overline{CO_2},\overline{DIC} \\ \overline{T},\overline{S}}}\right]^{-1} \cdot \left[\frac{\partial[CO_2]}{\partial TA}\Big|_{\substack{\overline{TA},\overline{H} \\ \overline{T},\overline{S}}}\delta TA\right. \\ & + \frac{\partial[CO_2]}{\partial[H^+]}\Big|_{\substack{\overline{TA},\overline{H} \\ \overline{T},\overline{S}}}\frac{\partial[H^+]}{\partial DIC}\Big|_{\substack{\overline{CO_2},\overline{DIC} \\ \overline{T},\overline{S}}}\delta DIC \\ & \left. + \Big(\frac{\partial[CO_2]}{\partial T}\Big|_{\substack{\overline{TA},\overline{H} \\ \overline{T},\overline{S}}} + \frac{\partial[CO_2]}{\partial[H^+]}\Big|_{\substack{\overline{TA},\overline{H} \\ \overline{T},\overline{S}}}\frac{\partial[H^+]}{\partial T}\Big|_{\substack{\overline{CO_2},\overline{DIC} \\ \overline{T},\overline{S}}}\Big)\delta T\right.\end{aligned}$$

$$+\Big(\frac{\partial[CO_2]}{\partial S}\Big|_{\overline{TA},\overline{H}}^{\overline{T},\overline{S}} + \frac{\partial[CO_2]}{\partial[H^+]}\Big|_{\overline{TA},\overline{H}}^{\overline{T},\overline{S}} \frac{\partial[H^+]}{\partial S}\Big|_{\overline{CO_2},\overline{DIC}}^{\overline{T},\overline{S}}\Big)\delta S\Big] \tag{7}$$

Comparing the terms from Eq.(7) to the desired Taylor's expansion:

$$\delta pCO_2 \approx \frac{\partial pCO_2}{\partial DIC}\Big|_{\overline{TA},\overline{DIC}}^{\overline{T},\overline{S}}\delta DIC + \frac{\partial pCO_2}{\partial TA}\Big|_{\overline{TA},\overline{DIC}}^{\overline{T},\overline{S}}\delta TA + \frac{\partial pCO_2}{\partial T}\Big|_{\overline{TA},\overline{DIC}}^{\overline{T},\overline{S}}\delta T + \frac{\partial pCO_2}{\partial S}\Big|_{\overline{TA},\overline{DIC}}^{\overline{T},\overline{S}}\delta S \tag{8}$$

We can identify the derivatives from Eq.(8), as follows:

$$
\begin{aligned}
\left.\frac{\partial pCO_2}{\partial TA}\right|_{\overline{T}A,\overline{S}}^{\overline{D}IC} &= \overline{pCO}_2 \cdot \frac{-\overline{TA}_c}{\overline{DIC}\cdot\Theta - \overline{TA}_c^2} \\
\left.\frac{\partial pCO_2}{\partial DIC}\right|_{\overline{T}A,\overline{S}}^{\overline{D}IC} &= \overline{pCO}_2 \cdot \frac{\Theta}{\overline{DIC}\cdot\Theta - \overline{TA}_c^2} \\
\left.\frac{\partial pCO_2}{\partial T}\right|_{\overline{T}A,\overline{S}}^{\overline{D}IC} &= \overline{pCO}_2 \cdot \frac{1}{\overline{DIC}\cdot\Theta - \overline{TA}_c^2}\left[\overline{TA}_c\cdot\left(\frac{\partial Alk_c}{\partial T}+\frac{\partial [B(OH)_4^-]}{\partial T}+\frac{\partial [OH^-]}{\partial T}\right)-\Theta\cdot\frac{\partial(DIC-[CO_2])}{\partial T}\right]-\frac{\overline{pCO}_2\cdot}{\overline{K_0}(T,S)}\frac{\partial K_0(T,S)}{\partial T} \\
\left.\frac{\partial pCO_2}{\partial S}\right|_{\overline{T}A,\overline{S}}^{\overline{D}IC} &= \overline{pCO}_2 \cdot \frac{1}{\overline{DIC}\cdot\Theta - \overline{TA}_c^2}\left[\overline{TA}_c\cdot\left(\frac{\partial \overline{TA}_c}{\partial S}+\frac{\partial [B(OH)_4^-]}{\partial S}+\frac{\partial [OH^-]}{\partial S}\right)-\Theta\cdot\frac{\partial(DIC-[CO_2])}{\partial S}\right]-\frac{\overline{pCO}_2\cdot}{\overline{K_0}(T,S)}\frac{\partial K_0(T,S)}{\partial S}
\end{aligned}
\tag{9}
$$

where $\Theta = [\mathrm{HCO_3^-}] + 4[\mathrm{CO_3^{2-}}] + \frac{[\mathrm{B(OH)_4^-}][\mathrm{H^+}]}{(\mathrm{k_b}+[\mathrm{H^+}])} + [\mathrm{H^+}] + [\mathrm{OH^-}]$ and $\overline{\mathrm{Alk_c}} = [\mathrm{HCO_3^-}] + 2[\mathrm{CO_3^{2-}}]$.

Below are some details of the specific concentrations derivatives.

$$
\begin{aligned}
\frac{\partial Alk_c}{\partial T,S} &= \frac{[CO_2]}{[H^+]^2}\left(\frac{\partial k_1}{\partial T,S}[H^+] + 2k_1\frac{\partial k_2}{\partial T,S} + 2k_2\frac{\partial k_1}{\partial T,S}\right) \\
\frac{\partial(DIC-[CO_2])}{\partial T,S} &= \frac{[CO_2]}{[H^+]^2}\left(\frac{\partial k_1}{\partial T,S}[H^+] + k_1\frac{\partial k_2}{\partial T,S} + k_2\frac{\partial k_1}{\partial T,S}\right) \\
\frac{\partial [B(OH)_4^-]}{\partial T} &= \frac{B_{tot}[H^+]}{(k_b+[H^+])^2}\frac{\partial k_b}{\partial T} \\
\frac{\partial [B(OH)_4^-]}{\partial S} &= \frac{B_{tot}[H^+]}{(k_b+[H^+])^2}\frac{\partial k_b}{\partial S} + \frac{k_b}{(kb+[H^+])}\frac{\partial B_{tot}}{\partial S} \\
\frac{\partial [OH^-]}{\partial T,S} &= \frac{1}{[H^+]}\frac{\partial k_w}{\partial T,S}
\end{aligned}
\tag{10}
$$

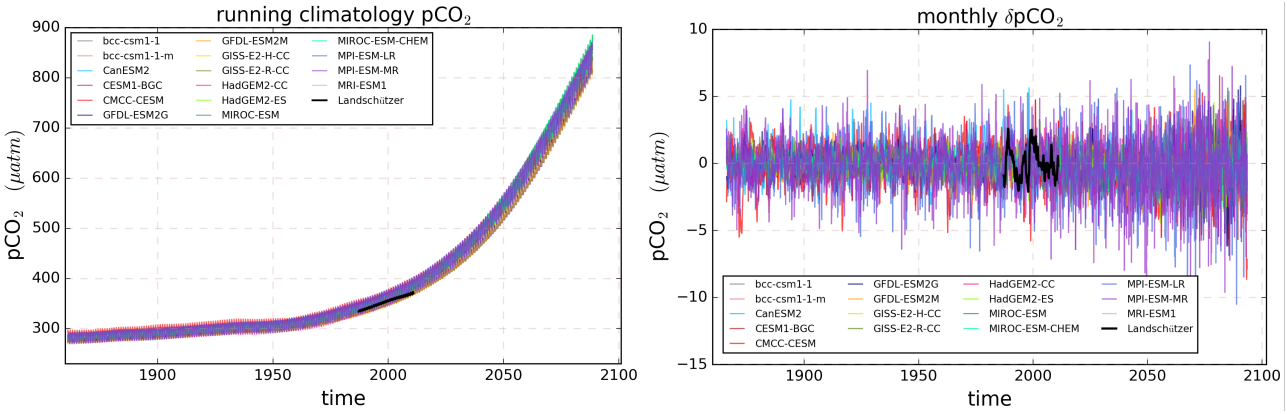

Figure S1. Time series (1866-2095) of pCO_2 as a) 11 years running climatology and b) monthly anomaly (calculated as the deviation from the climatology), for 13 different CIMP5 models, under RCP8.5 scenario. Overlaid in black is the anomalies from the observation-based estimations of Landschützer et al. (2017)

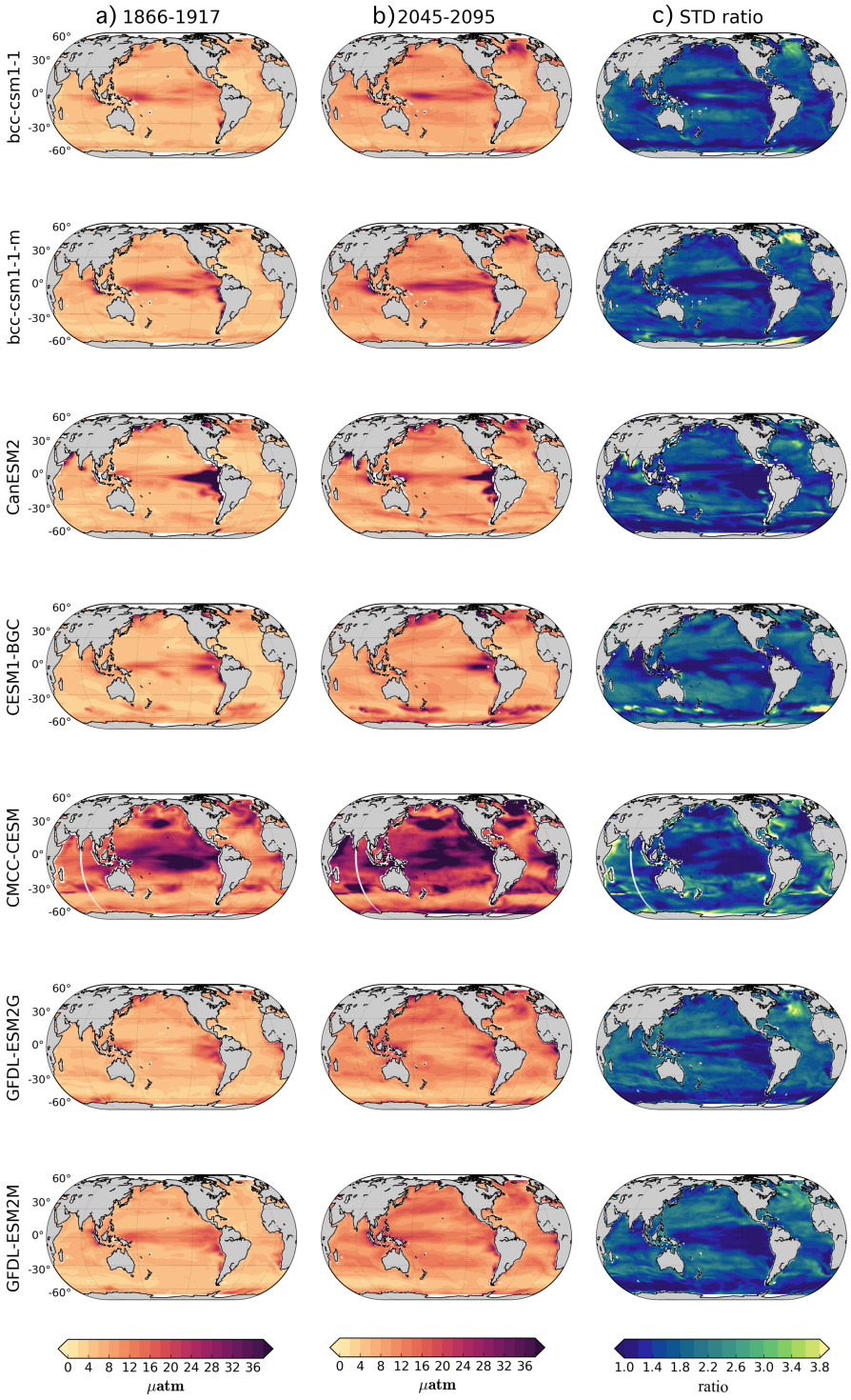

Figure S2. pCO_2's interannual anomalies, shown as a) 1866-1916 and b) 2045-2095 standard deviations. c) shows the 2045-2095 STD divided by 1866-1916 STD. Each row shows a different CMIP5 model.

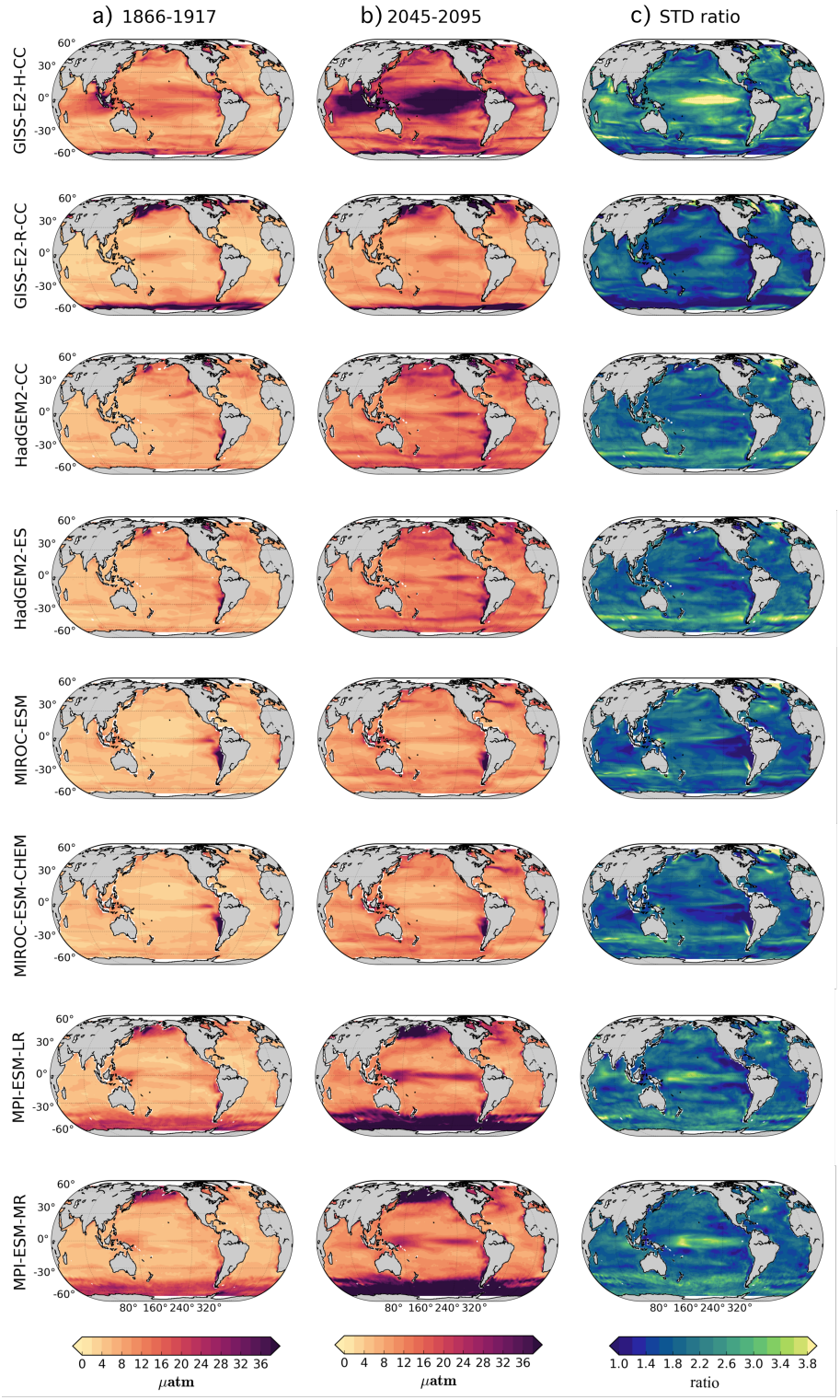

Figure S3. Same as Figure S2 but for different models.

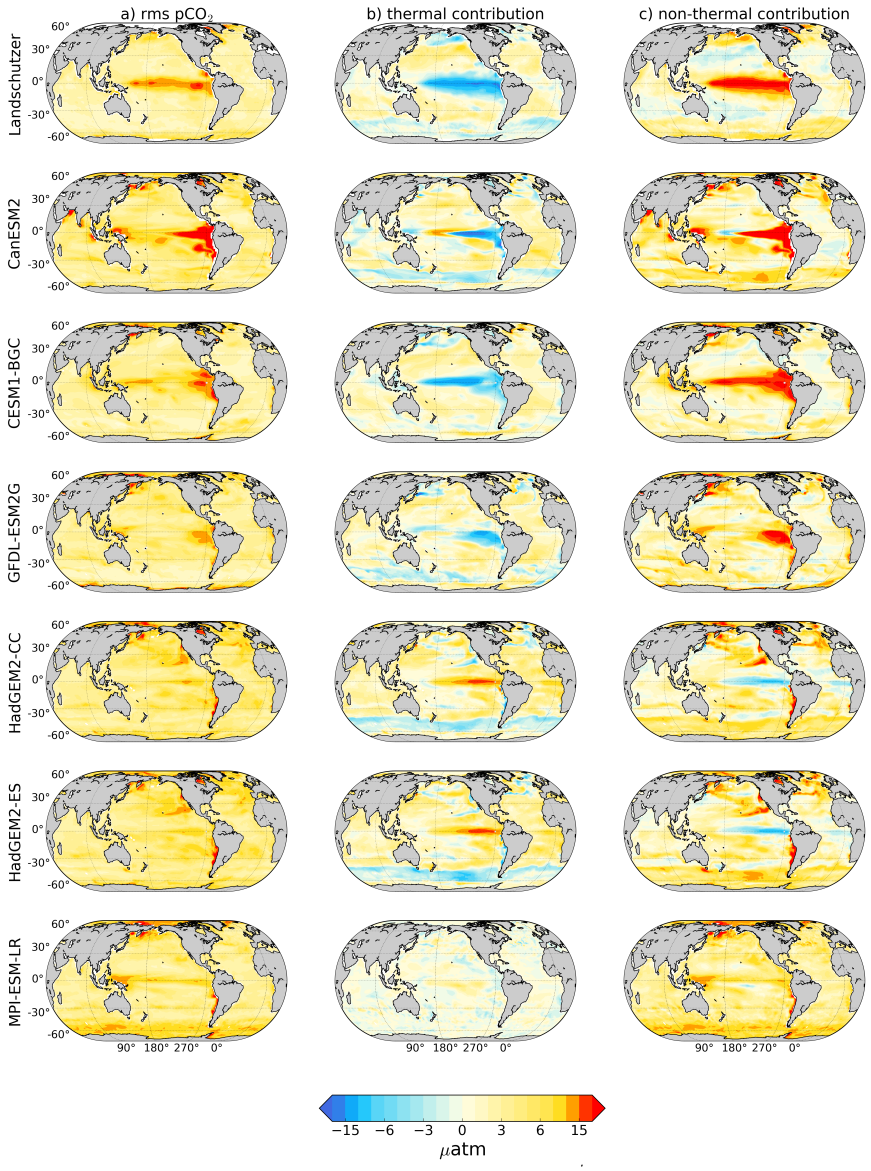

Figure S4. 1987-2010 values of root mean square (RMS) for a) pCO_2 anomalies and the b) thermal and c) non-thermal contributions to pCO_2's RMS. The contributions are defined as the regression coefficients between the components (either thermal or non-thermal) and the pCO_2 anomaly, following the method of Doney et al. (2009). The thermal and non-thermal components are calculated as Takahashi et al. (2002). The first row shows the observation-based results of Landschützer et al. (2017). The anomalies where calculated with the method of Landschützer et al. (2018), to compare with their results. The data was first filtered with a 12 month mean, and then detrended with a quadratic polynomial.

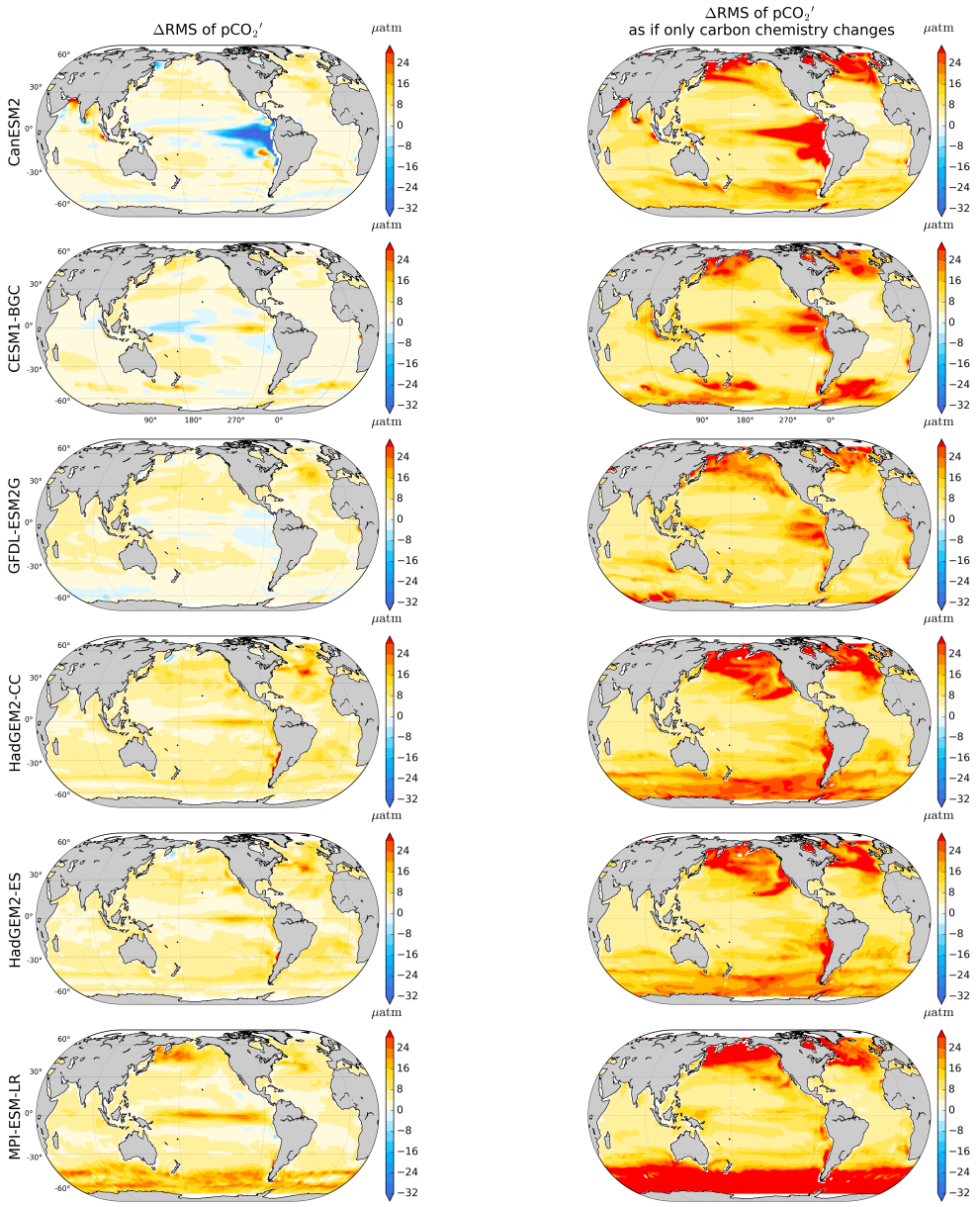

Figure S5. Causes of increasing pCO_2' variability: Total change (measured as 2045-2095 minus 1870-1920 values) of **a)** the RMS of pCO_2' and **b)** RMS of pCO_2' when only the value of $\overline{pCO_2}$, γ_{DIC_s} and γ_T vary, but we keep constant the 1870-1920 value of the DIC_s' and T' interannual anomalies. Each row represents a different model.

References

Dickson, A. G. (1990). Thermodynamics of the dissociation of boric acid in synthetic seawater

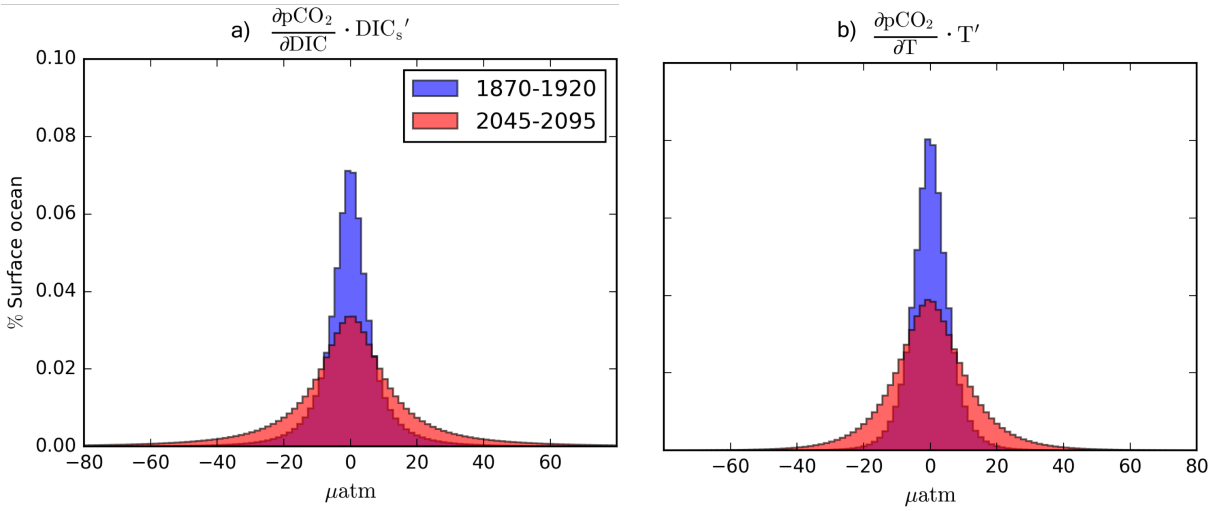

Figure S6. Increase on DIC_s and T contributions to pCO_2 interannual variability. **a)** and **b)** show the distributions of the DIC_s and T terms that control the pCO_2 anomalies, as calculated in Eq. (1) of the main text. The distributions show 600 monthly values for the 1870-1920 (blue) and 2045-2095 (red) periods for every point of the ocean between 180°E to 180°W and 60°S to 60°N.

from 273.15 to 318.15 K. *Deep-Sea Research Part A. Oceanographic Research Papers*, *37*, 755–766.

Doney, S. C., Lima, I., Feely, R. A., Glover, D. M., Lindsay, K., Mahowald, N., ... Wanninkhof, R. (2009). Mechanisms governing interannual variability in upper-ocean inorganic carbon system and air–sea CO_2 fluxes: Physical climate and atmospheric dust. *Deep Sea Research Part II: Topical Studies in Oceanography*, *56*(8), 640 - 655. doi: https://doi.org/10.1016/j.dsr2.2008.12.006

Egleston, E. S., Sabine, C. L., & Morel, F. M. M. (2010). Revelle revisited: Buffer factors that quantify the response of ocean chemistry to changes in DIC and alkalinity. *Global Biogeochem. Cycles*, *24*, GB1002.

Landschützer, P., Gruber, N., & Bakker, D. (2017). *An updated observation-based global monthly gridded sea surface pCO_2 and air-sea CO_2 flux product from 1982 through 2015 and its monthly climatology (NCEI Accession 0160558). Version 2.2. NOAA National Centers for Environmental Information. Dataset. doi:10.7289/v5z899n6.*

Landschützer, P., Gruber, N., Bakker, D. C. E., Stemmler, I., & Six, K. D. (2018). Strengthening seasonal marine CO_2 variations due to increasing atmospheric CO_2. *Nat. Clim. Change*, *8*, 146–150.

Millero, F. J. (1995). Thermodynamics of the carbon dioxide system in the oceans. *Geochemica et Cosmochemica Acta*, *59*, 661–677.

Millero, F. J., Graham, T. B., Huang, F., Bustos-Serrano, H., & Pierrot, D. (2006). Dissociation constants of carbonic acid in seawater as a function of salinity and temperature. *Marine Chemistry*, *100(1–2)*, 80–94.

Takahashi, T., Sutherland, S. C., Sweeney, C., Poisson, A., Metzl, N., Tilbrook, B., ... Nojiri,

Y. (2002). Global sea-air CO_2 flux based on climatological surface ocean pCO_2, and seasonal biological and temperature effects. *Deep-Sea Research II*, *49*, 1601–1623.